Astron. Astrophys. 346, 465–480 (1999)

ASTRONOMY AND ASTROPHYSICS

Impact of internal heating on the thermal evolution of neutron stars

Ch. Schaab[1], **A. Sedrakian**[2,⋆], **F. Weber**[1,3], **and M.K. Weigel**[4]

[1] Institut für theoretische Physik, Ludwig-Maximilians Universität, Theresienstrasse 37, D-80333 München, Germany
[2] Center for Radiophysics and Space Research, Cornell University, Ithaca, NY 14853, USA
[3] Nuclear Science Division, Lawrence Berkeley National Laboratory, Berkeley, CA 94720, USA
[4] Sektion Physik, Ludwig-Maximilians Universität, Am Coulombwall 1, D-85748 Garching, Germany

Received 26 October 1998 / Accepted 4 March 1999

Abstract. The impact of various competing heating processes on the thermal evolution of neutron stars is investigated. We show that internal heating leads to significantly enhanced surface temperatures for pulsars of middle and old age. The heating due to thermal creep of pinned vortices and due to outward motion of proton vortices in the interior of the star leads to a better agreement with the observed data in the case of enhanced cooling. The strong pinning models are ruled out by a comparison with the cooling data on the old pulsars. For millisecond pulsars, the heating due to thermal creep of pinned vortices and chemical heating of the core have the largest impact on the surface temperatures. The angular dependence of the heating rates require two dimensional cooling simulations in general. Such a simulation is performed for a selected case in order to check the applicability of one-dimensional codes used in the past.

Key words: stars: neutron – stars: evolution

1. Introduction

Simulations of the thermal evolution of neutron stars confronted with the soft X-ray and extreme UV observations of the photon flux emitted from their surface provide one of the most useful diagnostics of the physical processes operating in the dense interior of such stars. The early evolution of a neutron star is completely dominated by the cooling via neutrino emission; at this stage the star effectively radiates away the initial content of its thermal energy. In the later epoch one faces a competition between cooling and heating processes, where the heating may even dominate in the late stages of the thermal evolution. Eventually, they reach a thermal equilibrium phase, where the heat generated in the star is radiated away at the same rate from the stellar surface.

The relative importance of the various elementary processes contributing to cooling is fairly well understood (e.g. Richardson et al. 1982; Van Riper 1991; Umeda et al. 1994; Schaab et al. 1996; Page 1998). The investigations performed so far have however the deficit that they did not sufficiently clarify the relative weight of the different heating processes. The majority of these investigations concentrated on few preferred dissipation processes (e.g Shibazaki & Lamb 1989; Cheng et al. 1992; Sedrakian & Sedrakian 1993; Reisenegger 1995) with the exception of the work of Van Riper (1991), who treats the heating in general phenomenological terms. A meaningful comparison of the individual processes studied in these papers is strongly hampered by the fact that these investigations were performed for different microphysical inputs and different levels of sophistication concerning the cooling simulation code, preventing one from drawing definitive conclusions about the relative importance of the individual heating processes.

The aim of this paper is a comparative analysis of the impact of different heating processes on the thermal evolution of neutron stars. Our simulations take into account the most recent developments concerning the microphysical input and employ both relativistic and non-relativistic equations of state of superdense matter. We perform the cooling calculations for a fully relativistic, evolutionary simulation code. Although internal heating is generally azimuthally asymmetric, we shall use an one-dimensional cooling code for almost all simulations. To demonstrate the reliability of this approximation, a two-dimensional calculation is performed for a selected case as well (Schaab & Weigel 1998). As far as we know, this is the first fully two-dimensional simulation of neutron star cooling which takes internal heating into account.

The heating processes emerge as a response to the loss of rotational energy of the star and can be divided roughly into two groups. Firstly, processes caused by the readjustment of the equilibrium structure of the compact object such as a sequence of crust/core-quakes (Cheng et al. 1992 and references therein); nuclear reactions in cold nuclear matter with non-equilibrium composition (picno-nuclear reactions in the crust and weak processes in the core, see, e.g., Iida & Sato 1997 and Reisenegger & Goldreich 1992). Secondly, processes related to superfluidity such as dissipative motion of the neutron vortex lattice in the superfluid crusts (Shibazaki & Lamb 1989; Link & Epstein 1991;

Send offprint requests to: Ch. Schaab (schaab@gsm.sue.physik.uni-muenchen.de)

⋆ *Present address:* Kernfysisch Versneller Instituut, Zernikelaan 25, 9747 AA Groningen, The Netherlands

Bildsten & Epstein 1989; Jones 1990) and the dissipative motion of proton vortex lattice in the superfluid core and the vorticity decay at the phase separation boundaries, e.g. at the crust-core interface, (Sedrakian & Sedrakian 1993; Sedrakian & Cordes 1998b).

The rate of dissipation associated with these processes is, in most cases, intimately connected with the spin evolution of the star, in particular the evolution of its magnetic moment. The time dependence of the magnetic moment and the moment of inertia will affect the heating rate and thus the star's cooling behaviour along with the relation between the luminosity and the age of the star; these effects are ignored in this study in order to constrain the actual number of the evolutionary scenarios; we shall assume therefore a constant magnetic moment and moment of inertia.

The paper is organised as follows. The equations of thermal and rotational evolution of a neutron star are given in Sect. 2. Various heating processes associated with the dissipative motion of vortices and the changes of the equilibrium structure are reviewed in Sects. 3 and 4. Additional physical input is discussed in Sect. 5. The observed data are summarised in Sect. 6. Sect. 7 presents the results of our cooling simulations which are discussed in Sect. 8.

2. Thermal and rotational evolutions

2.1. Equations of thermal evolution

The thermal evolution is governed by the coupled system of equations for energy balance (Thorne 1977),

$$\frac{\partial(L\mathrm{e}^{2\phi})}{\partial r} = 4\pi r^2 \mathrm{e}^{\Lambda}\left(-\epsilon_\nu \mathrm{e}^{2\phi} + h\mathrm{e}^{2\phi} - c_\mathrm{v}\frac{\partial(T\mathrm{e}^{\phi})}{\partial t}\right), \qquad (1)$$

and thermal energy transport,

$$\frac{\partial(T\mathrm{e}^{\phi})}{\partial r} = -\frac{(L\mathrm{e}^{2\phi})\mathrm{e}^{\Lambda-\phi}}{4\pi r^2\kappa}. \qquad (2)$$

This system requires as a microphysical input the neutrino emissivity per unit volume, $\epsilon_\nu(\rho,T)$, the heat rate per unit volume, $h(\rho,T,\Omega,\dot{\Omega})$, the heat capacity per unit volume, $c_\mathrm{v}(\rho,T)$, and the thermal conductivity, $\kappa(\rho,T)$, where ρ is the local density. The g_{tt} and g_{rr} components of the Schwarzschild metric tensor $\mathbf{g}$ are denoted by $-\mathrm{e}^{2\phi}$ and $\mathrm{e}^{2\Lambda}$, respectively, L is the luminosity, and the other variables have their usual meaning. The boundary conditions for (1) and (2) read

$$L(r=0) = 0, \qquad (3)$$

$$T(r=r_\mathrm{m}) = T_\mathrm{m}(r_\mathrm{m}, L_\mathrm{m}, M_\mathrm{m}), \qquad (4)$$

where $T_\mathrm{m}(r_\mathrm{m}, L_\mathrm{m}, M_\mathrm{m})$ is fixed by the properties of the photosphere at the density $\rho = \rho_\mathrm{m} = 10^{10}\,\mathrm{g\,cm^{-3}}$ (Gudmundson et al. 1983). Since the star's thermal evolution for times greater than, say, a few months does not depend on the detailed initial temperature profile in the interior of the star, one can choose, without loss of generality, an initialy isothermal temperature distribution of $T(r) \equiv 10^{11}$ K. The set of equations for thermal evolution (1) and (2) were solved numerically by means of a Newton-Raphson type algorithm. The microphysical input quantities needed for the solution of these equations are given in Table 1 and will be discussed in detail in Sect. 5. If one accounts for azimuthal asymmetry of the input quantities, e.g. the heat rate h, one has to solve two-dimensional thermal evolution equations, which have already been presented in Schaab & Weigel (1998) Schaab98c along with the numerical method for solving them.

2.2. The normal component

We shall start the discussion of the rotational evolution by a brief review of the spin dynamics of the normal (non-superfluid) component of the star. The combined effect of the braking of the star's rotation via the emission of electromagnetic radiation, electron-positron wind, and gravitational waves on the spin evolution is commonly cast in a generic power-law form

$$\dot{\Omega}_\mathrm{c}(t) = -K(t)\Omega_\mathrm{c}^n(t), \qquad (5)$$

where Ω_c is the spin frequency of the normal component. The functional form of $K(t)$ and $n(t)$ depends on the dominant process assumed. If one assumes that the energy losses are due to the magnetic dipole radiation (Goldreich et al. 1971), then $n = 3$ and K is a function of the surface magnetic field strength B, the angle α between spin and magnetic axis, the moment of inertia of the star I, and a correction factor $\gamma \equiv 1 + \mathrm{d}\ln I/\mathrm{d}\ln\Omega_\mathrm{c}$:

$$K \propto \frac{B^2\sin^2\alpha}{\gamma I}. \qquad (6)$$

The braking index is known for the four youngest pulsars for which the measurements of the second time derivative of the period, P, are available (Lyne et al. 1993, Kaspi et al. 1994, Boyd et al. 1995). All four braking indices given by $n = P\ddot{P}/\dot{P}^2$ fall into the range between 1.2 and 2.8. The deviations from the value for the magnetic dipole radiation has been attributed to the increase of the surface magnetic field strength (Blandford et al. 1983, Muslimov & Page 1996), an increase of the angle between the spin and magnetic moment axis (Beskin et al. 1984, Link & Epstein 1997), or presence of the weakly coupled superfluid in the core of the star (Sedrakian & Cordes 1998a). We shall assume, in a first approach to the problem, K to be constant and $n = 3$.

With these assumptions, integration of Eq. (5) yields

$$\Omega_\mathrm{c}(t) = \left((n-1)Kt + \Omega_\mathrm{i}^{-(n-1)}\right)^{-1/(n-1)}, \qquad (7)$$

where Ω_i is the initial angular velocity at $t = 0$. If the initial angular velocity is large compared to the present angular velocity, Eq. (7) simplifies to

$$\Omega_\mathrm{c}(t) = \left((n-1)Kt\right)^{-1/(n-1)}, \qquad (8)$$

and the age of the pulsar can be expressed as

$$t = \frac{1}{n-1}\frac{\Omega_\mathrm{c}(t)}{|\dot{\Omega}_\mathrm{c}(t)|}. \qquad (9)$$

Apart from affecting the cooling history, the time variation of K, as well as a deviation of the braking index from its canonical value, $n = 3$, may lead to over- or underestimating the true age by a factor as large as 3. A comparison of the theoretical cooling tracks with observed data is therefore affected by this uncertainty (see Sect. 6).

2.3. The superfluid component

The angular velocity of the superfluid phases adjusts to the changes in the rotation rate of the normal component via expansion or contraction of the neutron vortex lattice, which carries the angular momentum of the superfluid. The mean macroscopic density of neutron vortex lines $n_{\rm l}$ in cylindrical coordinates $(r_{\rm p}, z, \phi)$ is given by the Feynman-Onsager quantisation condition

$$\kappa n_{\rm l}(r_{\rm p}, t) = 2\Omega_{\rm s}(r_{\rm p}, t) + r_{\rm p}\frac{\partial \Omega_{\rm s}(r_{\rm p}, t)}{\partial r_{\rm p}}. \quad (10)$$

$\Omega_{\rm s}(r_{\rm p})$ denotes the angular velocity of the superfluid component and $\kappa = h/2m_{\rm N}$ is the quantum of circulation carried by each vortex, where h denotes the Planck constant and $m_{\rm N}$ is the bare neutron mass. The second term accounts for the gradients in the distribution of vortex lines. Because of the lack of sources and sinks for vortex lines in the bulk of the superfluid, the temporal evolution of the vortex number density obeys the number conservation law:

$$\frac{\partial n_l}{\partial t} + \boldsymbol{\nabla} \cdot (n_l \boldsymbol{v}_l) = 0, \quad (11)$$

where $\boldsymbol{v}_l$ is the velocity of vortex lines. Combination of Eqs. (10) and (11) leads to

$$\frac{\partial \Omega_{\rm s}}{\partial t} = -\frac{1}{r_{\rm p}}\kappa n_{\rm l} v_{\rm l}^{\rm r} = -\left(\frac{2}{r_{\rm p}}\Omega_{\rm s} + \frac{\partial \Omega_{\rm s}}{\partial r_{\rm p}}\right) v_{\rm l}^{\rm r}. \quad (12)$$

A decrease of the spin of the superfluid component ($\dot{\Omega}_{\rm s} < 0$) causes an outward radial velocity $v_{\rm l}^{\rm r} > 0$. In the following we neglect the second term in parentheses and assume $\Omega_{\rm s}(r_{\rm p})$ to be constant throughout the superfluid phase, since the vorticity gradients depend on the density profile of the mutual friction coefficients, which are poorly known. Furthermore, over the evolutionary timescale one can assume that $\dot{\Omega}_c = \dot{\Omega}_{\rm s}$, i.e. the deceleration rates of the superfluid and the normal components are the same. Then the velocity of the radial motion of the vortices (and therefore the rate of dissipation) are related to the spin-down characteristics of the normal component via Eq. (12). In this manner the dynamics of superfluid phases is eliminated from the system of coupled equations of secular and thermal evolution, and the heating rates are given directly in terms the spin characteristics of the normal component.

3. Dissipative motion of vortex lattices

We next turn to the description of the dissipation processes included in the thermal evolution simulations. A number of dynamical coupling regimes has been suggested in the literature for the coupling of the superfluid component to the crusts. We shall discuss several variants of the two main alternatives - the pinned and the corotation regimes.

3.1. Vortex pinning at nuclei

The vortex creep theories of the dynamics of neutron vortices in the inner crust assume these vortices to be pinned to the nuclear lattice (Anderson & Itoh 1975, Alpar 1977, Alpar et al. 1984, Epstein & Baym 1988, Link & Epstein 1991, Pizzochero et al. 1997). The pinning force provides a large resistive force to the vortex motion which is necessary to spin down the superfluid component. In this regime, the vortices move due to the process of vortex creep, i.e. by thermal activation from one pinning configuration to another. The vortex creep rate has the general form (Link et al. 1993)

$$v_{\rm l}^{\rm r} = v_0 {\rm e}^{-A/T_{\rm eff}}, \quad (13)$$

where v_0 is a microscopic velocity, A denotes the activation energy for a segment of a vortex line to overcome its pinning barrier, and $T_{\rm eff}$ is the effective temperature which includes quantum tunnelling effects and is a function of the local temperature of the thermal bath. These quantities depend on microscopic parameters (e.g. the pinning energy), which themselves depend on the density, and on the velocity difference between the superfluid and the normal component δv^ϕ. Since the creep rate $v_{\rm l}^{\rm r}$ is given by Eq. (12), Eq. (13) has to be inverted to obtain the velocity difference δv^ϕ. This is done by an iterative procedure similar to the one described by Van Riper et al. (1995) .

The rotational energy of the superfluid is converted to thermal energy by the radial motion of the vortices. The energy dissipated by a single vortex per unit time is $\dot{E}_{\rm diss} = f_{\rm M}^{\rm r} v_{\rm l}^{\rm r}$, where $f_{\rm M}^{\rm r} = \rho_{\rm s}\kappa\delta v^\phi$ is the radial component of the Magnus force. The dissipated energy h per unit time and volume is then given by:

$$h = \dot{E}_{\rm diss} n_{\rm l} = r_{\rm p}\rho_{\rm s}\delta v^\phi |\dot{\Omega}_{\rm s}|, \quad (14)$$

where Eq. (12) has been used. The integration over the volume of the superfluid component gives:

$$\int h {\rm d}V = |\dot{\Omega}_{\rm s}| \int \rho_{\rm s} r_{\rm p} \delta v^\phi {\rm d}V. \quad (15)$$

This result guarantees conservation of both energy and angular momentum. For the implementation of h in our one-dimensional cooling code, h has to be averaged over spherical shells:

$$\bar{h} = \frac{\int h \sin\theta {\rm d}\theta {\rm d}\phi}{4\pi} = \frac{1}{4}\pi r \rho_{\rm s} \delta v^\phi |\dot{\Omega}_{\rm s}|, \quad (16)$$

where we assumed that δv^ϕ is approximately constant on spherical shells. This approximation seems to be reliable because δv^ϕ depends only logarithmically on $r_{\rm p}$ (Van Riper et al. 1995).

We shall consider two models for pinning: the first model (EB) uses the parameters from Epstein & Baym (1988) and Link & Epstein (1991) , where the pinning energy is derived

from the Ginzburg-Landau theory. In the second model (PVB) the parameters are derived by Pizzochero et al. (1997) from the Bardeen-Cooper-Schrieffer theory of superconductivity. Below the density $1.5 \times 10^{13}\,\mathrm{g\,cm^{-3}}$ the parameters for the both models do not deviate considerably. However, above densities $\gtrsim 1.5 \times 10^{13}\,\mathrm{g\,cm^{-3}}$ the large deviations in the pinning energy (the typical pinning energy is $\sim 10\,\mathrm{MeV}$ in the EB model and $\sim 1\,\mathrm{MeV}$ in the PVB model) leads to rather different evolutionary scenarios and, therefore, we shall treat both models seperately.

3.2. Corotating regime in the crust

The dynamics of the neutron vortices in the corotating regime is governed by the force balance equation

$$\boldsymbol{f}_\mathrm{M} + \boldsymbol{f}_\mathrm{d} = 0, \tag{17}$$

where the Magnus and the drag (resistive) forces are:

$$\boldsymbol{f}_\mathrm{M} = -\rho_s \boldsymbol{\kappa} \times (\boldsymbol{v}_\mathrm{s} - \boldsymbol{v}_\mathrm{l}), \tag{18}$$
$$\boldsymbol{f}_\mathrm{d} = -\eta(\boldsymbol{v}_\mathrm{l} - \boldsymbol{v}_\mathrm{c}), \tag{19}$$

with the drag coefficient η. A decomposition of the force balance equation into radial and azimuthal components gives

$$\boldsymbol{v}_\mathrm{l} = (v_\mathrm{s} - v_\mathrm{c}) \sin\theta_\mathrm{d} \cos\theta_\mathrm{d} \boldsymbol{e}_r + (v_\mathrm{s} + v_\mathrm{c} \tan^2\theta_\mathrm{d}) \cos^2\theta_\mathrm{d} \boldsymbol{e}_\phi, \tag{20}$$

where the dissipation angle θ_d, following Bildsten & Epstein (1989), is defined as

$$\tan\theta_\mathrm{d} = \frac{\eta}{\rho_\mathrm{s}\kappa}. \tag{21}$$

The rate of the dissipation per unit volume is then given by

$$h = -\boldsymbol{f}_\mathrm{d} \cdot (\boldsymbol{v}_\mathrm{l} - \boldsymbol{v}_\mathrm{c}) n_\mathrm{free} = \rho_\mathrm{s} r_\mathrm{p}^2 |\dot{\Omega}_\mathrm{s}| \omega, \tag{22}$$

with the abbreviation

$$\omega = \frac{v_\mathrm{s} - v_\mathrm{c}}{r} = \frac{v_\mathrm{l}^\mathrm{r}}{r_\mathrm{p} \sin\theta_\mathrm{d} \cos\theta_\mathrm{d}}, \tag{23}$$
$$= -\frac{\dot{\Omega}_\mathrm{s}}{2\Omega_\mathrm{s}} \frac{1}{\Phi_\mathrm{free}} \frac{1}{\sin\theta_\mathrm{d} \cos\theta_\mathrm{d}}. \tag{24}$$

Here, Φ_free denotes the fraction of the free (corotating) vortices. This quantity is largely unknown, but for stationary situations, one may assume that definite crustal regions support either corotation or creep regimes and the mixing is small. Hence we shall adopt $\Phi_\mathrm{free} := n_\mathrm{free}/n_\mathrm{l} = 1$ for the corotating regime.

The dominant processes in this regime result from the coupling of the translational motion of the vortices to the electron-phonon system (Jones 1990). The leading order coupling implies a resistive force constant

$$\eta_0 \simeq \frac{3}{32\pi^{1/2}} \frac{a\,E_p^2}{M \xi_n^3 c_s^3}, \tag{25}$$

where a is the lattice constant, E_p the pinning energy, ξ_n the neutron coherence length, M the (effective) mass of the nuclei, and c_s the phonon velocity (given by the unperturbed dispersion relation). Using Eq. (25) we find $\eta_0 \sim 10^5\ \mathrm{g\ cm^{-1}\,s^{-1}}$ at the density $\rho_s = 10^{13}\,\mathrm{g\ cm^{-3}}$ and, therefore, $\tan\theta_d \sim 5 \times 10^{-6}$. The processes corresponding to higher orders in the vortex displacement are generally velocity dependent. The next-to-leading order term, involving one-phonon processes, is estimated as (Epstein & Baym 1992, Jones 1992)

$$\eta_1 \simeq \frac{E_p^2}{2\rho_s \omega a \xi_n^2 \sqrt{2\pi\xi_n c_K v_L^3}}, \tag{26}$$

where c_K is the kelvon velocity due to excitation of the oscillatory degrees of freedom of the vortex lines moving with velocity v_L. This process is sensitive to the actual excitation spectrum of kelvons. The possible localisation of kelvons in a random nuclear potential (Jones 1992) leads to a threshold in the excitation spectrum beyond which a continuum of states becomes available for excitations. In addition one requires knowledge of the scattering amplitudes beyond the Born approximation. For typical parameters one finds $\eta_1 \sim 10^{10}\,\mathrm{g\,cm^{-1}\,s^{-1}}$ at a density of $\rho_s \sim 10^{13}\,\mathrm{g\,cm^{-3}}$, and, therefore, $\tan\theta_d \sim 1$. However, in the stationary situations, the vortex velocities are rather small, and we shall assume that the leading term η_0 is the dominant one in the corotating regime.

3.3. Electron–vortex scattering in superfluid core

An estimate of the heating processes in the superfluid core requires knowledge of vortex lattice structure that nucleates after the superfluid phase transition. We shall pursue the point of view that the core's magnetic field nucleates in a proton vortex lattice. The frictional forces in a neutron star's core are dominated by the scattering of the quasiparticle excitations of the electron normal Fermi-liquid by the proton vortex lattice. The reason is that the number of proton vortices per neutron vortex, given by $n \simeq (\sqrt{3}/2)(B/\Phi_0)d_n^2$, is of the order of $n \geq 10^{12}$ for $B \sim 10^{12}$ G and a neutron vortex lattice constant of $d_n \sim 10^{-3}$ cm. The dominant dissipative scattering results from the scattering of electron excitations off the quasiparticle excitations confined in the core of proton vortex lines. The scattering rate is a sensitive function of the form-factor of the vortex line core and the actual distribution of vortex lines (e.g. formation of vortex clusters, Sedrakian & Cordes 1998b). An order-of-magnitude estimate of the dissipation rate is given by (Sedrakian & Sedrakian 1993)

$$h = \frac{45}{8\pi} f T \left(\frac{\dot{\Omega}}{\Omega}\right)^2 R^2 \sin^2\theta \cos^2\theta, \tag{27}$$

where T is the temperature, R the radius of the superfluid core and f is defined as[1].

$$f = 41\pi^2 \alpha^2 \frac{m_\mathrm{p}^2 k_\mathrm{B}}{\hbar^3 c} \frac{k_\mathrm{F}}{k_\mathrm{FT}} \frac{\Delta_\mathrm{p} E_\mathrm{p}}{\hbar} |k| \left(\frac{\xi_\mathrm{p}}{\lambda_\mathrm{p}}\right)^{2+2/3|k|}$$

[1] Note that the multiplication sign in the second line of Eq. (11) in Sedrakian & Sedrakian (1993) should be replaced by a division sign. This misprint is corrected here.

$$\times \left(\frac{2m_{\rm p}c^2}{E_{\rm p}}\right)^{1/2} \exp\left(-\frac{0.78\Delta_{\rm p}^2}{E_{\rm p}k_{\rm B}T}\right), \quad (28)$$

where $k_{\rm F} = (3\pi^2 n_{\rm p})^{1/3}$ denotes the proton Fermi momentum, $k_{\rm FT} = \left(4k_{\rm F}m_{\rm p}e^2/\pi\hbar^2\right)^{1/2}$ the Thomas-Fermi screening length, $E_{\rm p} = \hbar^2 k_{\rm F}^2/2m_{\rm p}^*$ the proton quasiparticle energy with the proton effective mass $m_{\rm p}^*$, $k \equiv (m_{\rm p}^* - m_{\rm p})/m_{\rm p}$ the entrainment coefficient, and

$$\xi_{\rm p} = \frac{\hbar^2 k_{\rm F}}{\pi m_{\rm p}\Delta_{\rm p}}, \quad (29)$$

$$\lambda_{\rm p} = (1+|k|)^{1/2}\left(\frac{m_{\rm p}c^2}{4\pi n_{\rm p}e^2}\right)^{1/2} \quad (30)$$

the proton coherence length and the magnetic field penetration length, respectively. It should be noted that the dynamical coupling of the proton vortex clusters to the electron liquid is controlled by the electron flux-scattering processes, whose rate is larger than that for the electron scattering off the vortex core quasiparticles. While in the latter case the scattering is inelastic (i.e. energy is transfered to the proton quasiparticle localised in the vortex core), the former process of electron-flux scattering is predominantly elastic i.e. involves only a change of direction of the electron momentum (but no changes in the energy). In the classical (or quasi-classical) limit this process corresponds to the bending of the electron trajectory in the magnetic field of a vortex under the action of the Lorentz force and is manifestly non-dissipative. In the quantum limit the processes of the soft-photon emission can not be dismissed in general; however the corresponding rates should be substantially less than the elastic scattering rates.

3.4. Decay of vortices

The proton vortices, which are dragged along by the neutron vortex motion in the radial outward direction to the crust–core boundary, would decay as they merge in the crust, thus releasing their self-energy. The relevant crust-core boundary for this process should be identified with the phase transition point between the phase with protons bound in heavy nuclei and the phase in which they are in continuum states. Since the crustal matter can not support a proton supercurrent, the circulation currents of proton vortices would decay on the ohmic dissipation timescale, which is much smaller than a star's spin-down time scale. The resulting heating rate at the crust-core boundary is given by

$$\int h{\rm d}V = g\frac{|\dot{\Omega}|}{\Omega}R^3, \quad (31)$$

with

$$g = \frac{1}{3}\left(1-\left(2\ln\frac{\lambda_{\rm p}}{\xi_{\rm p}}\right)^{-1}\right)|k|\left(\frac{\xi_{\rm p}}{\lambda_{\rm p}}\right)^{2/3|k|} \times \left(\frac{\Phi_0}{4\pi\lambda_{\rm p}}\right)^2 \ln\frac{\lambda_{\rm p}}{\xi_{\rm p}}\,. \quad (32)$$

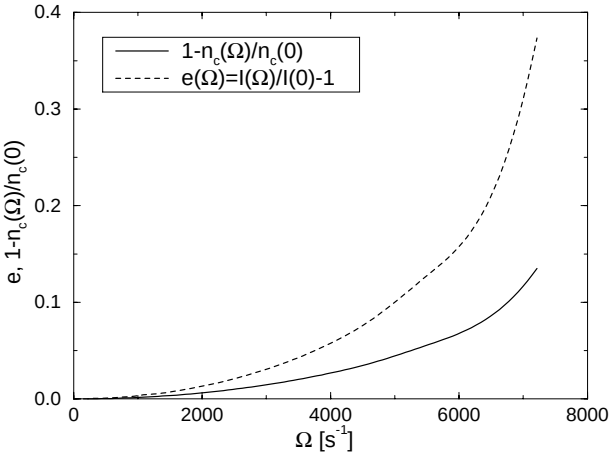

Fig. 1. Oblateness e and the variation of the central density $1 - n_{\rm c}(\Omega)/n_{\rm c}(0)$ of rotating neutron stars versus angular velocity. The parameters are: $M_{\rm B} = 1.58M_\odot$ and UV_{14}+UVII-EOS.

Here, $\Phi_0 = hc/2e$ is the flux quantum. The quantity g is very sensitive to variations of the microphysical parameters such as the proton density, the effective mass, and the gap energy at the location of the phase transition point. We use a fixed upper limit for this process corresponding to the value of $g = 10^{28}$.

4. Readjustment to equilibrium structure

As a neutron star spins down its global structure readjusts itself toward a more spherically symmetric configuration to minimise the sum of gravitational and rotational energy. Two models of internal heating discussed here are based on the structural readjustment of the oblateness of the star, defined as

$$e_{\rm eq} := \frac{I(\Omega)}{I(0)} - 1, \quad (33)$$

and of the central baryon density $n_{\rm c}$. $I(\Omega)$ denotes the star's moment of inertia. The equilibrium values of both quantities are determined as functions of the angular velocity by computing a sequence of rotating neutron star models with constant baryon number (Schaab 1999). These calculations are done by solving the general relativistic stellar structure equations in two dimensions, in a similar manner as in Komatsu et al. (1989) and Bonazzola et al. (1993). As an example the oblateness e and the fraction $1 - n_{\rm c}(\Omega)/n_{\rm c}(0)$ with the central density $n_{\rm c}(\Omega)$ are plotted for a neutron star model with constant baryon mass $M_{\rm B} = 1.58M_\odot$ in Fig. 1. The underlying equation of state is the non-relativistic UV_{14}+UVII-model (see Sect. 5.1).

4.1. Crust cracking

If both the interior and the crust are liquid, the oblateness will continuously adjusts itself to the equilibrium value. This is the case for the temperatures $T \gtrsim 10^8$ K (Cheng et al. 1992). However, if the crust solidifies, the oblateness continuously depart

from its equilibrium value causing an increasing mean stress on the crust according to (Baym & Pines 1971)

$$\sigma = \tilde{\mu}(e - e_{\rm eq}), \tag{34}$$

where $\tilde{\mu}$ is the mean shear modulus of the crust. The quantity $e_{\rm eq}$ refers to the equilibrium value of the oblateness. If the mean stress σ reaches some critical value

$$\sigma_{\rm c} = \tilde{\mu}\theta_{\rm c}, \tag{35}$$

the crust breaks and the deviation of e from its equilibrium value is reduced. For an ideal Coulomb lattice, the value of the critical shear angle $\theta_{\rm c}$ is of the order of magnitude $10^{-1} - 10^{-2}$ (Smolukowski & Welch 1970). The fraction of impurities or defects in the neutron star crusts could be considerable due to, e.g., the fast cooling below the melting temperature of the lattice. Smolukowski & Welch (1970) argues that the value of $\theta_{\rm c}$ is then reduced to roughly $10^{-4} - 10^{-5}$.

During the breaking of the crust the strain energy

$$\Delta E_{\rm strain} = 2B(e - e_{\rm eq})\Delta(e - e_{\rm eq}) \tag{36}$$

is released (Cheng et al. 1992), where $\Delta(e-e_{\rm eq}) \ll (e-e_{\rm eq})$ is the change in $(e - e_{\rm eq})$, and the coefficient B is given in terms of the mean shear modulus by $B = \frac{1}{2}V_{\rm c}\tilde{\mu}$ with $V_{\rm c}$ being the volume of the crust. We follow Cheng et al. (1992) in assuming that $(e - e_{\rm eq})$ is approximately equal to its maximum value $\theta_{\rm c}$ and that the time Δt between two successive quakes is small compared to the time scale of thermal evolution. Hence[2]

$$\begin{aligned}\frac{{\rm d}E_{\rm strain}}{{\rm d}t} &\approx \frac{\Delta E_{\rm strain}}{\Delta t} = 2B\theta_{\rm c}\frac{\Delta(e - e_{\rm eq})}{\Delta t} \\ &\approx -2B\theta_{\rm c}\frac{{\rm d}e_{\rm eq}}{{\rm d}\Omega_{\rm c}}\dot{\Omega}_{\rm c}.\end{aligned} \tag{37}$$

The crust strength B is given by the integral (Baym & Pines 1971)

$$B = \int_{V_{\rm c}} b(r){\rm d}^3 r \tag{38}$$

with

$$b(r) = \frac{1}{25}C_{44}(r)\left(96 - 166\left(\frac{r}{R}\right)^2 + \frac{777}{10}\left(\frac{r}{R}\right)^4\right) \tag{39}$$

and the shear modulus of a bcc-lattice (Mott & Jones 1936)

$$C_{44}(r) = 0.3711Z^2e^2n_{\rm N}\left(\frac{2}{n_{\rm N}}\right)^{-1/3}. \tag{40}$$

The total strain energy release (37) can thus be expressed in terms of a local energy loss rate:

$$h = 2b\theta_{\rm c}\frac{{\rm d}e_{\rm eq}}{{\rm d}\Omega_{\rm c}}|\dot{\Omega}_{\rm c}|. \tag{41}$$

[2] Our formulas differ from those of Cheng et al. (1992) by a factor $\theta_{\rm c}/e$, which is $\ll 1$ for slowly rotating stars. We therefore obtain no effect on the cooling of slowly rotating stars, in contrast to Cheng et al. (1992) where rather large effects are claimed.

4.2. Chemical heating

The central density of a rotating neutron star with fixed baryon number depends on the angular velocity (see Fig. 1). As the star spins down, the centrifugal force decreases and correspondingly the central density increases (by up to 20%). This is accompanied by a shift of the chemical equilibrium. The matter would maintain chemical equilibrium if the relaxation timescales for the weak processes are small compared to the timescale of rotational evolution. However, these timescales are found to be comparable and the actual composition departs from chemical equilibrium, which modifies the reaction rates (Haensel 1992) and usually leads to a net conversion of chemical energy into thermal energy (Reisenegger & Goldreich 1992, Iida & Sato 1997).

For simplicity we restrict ourselves to a system containing only neutrons, protons, electrons, and muons in β-equilibrium (as is described by the non-relativistic EOS UV$_{14}$+UVII). The equation of state of cold, charge neutral matter, which is not necessarily in β-equilibrium (we assume however equal chemical potentials for electrons and muons: $\mu_{\rm e} = \mu_{\mu}$.), therefore depends only on two parameters. These are chosen to be the baryon density n and the relative proton density $x = n_{\rm p}/n$. These two parameters are constant on closed, sphere-like surfaces $\mathcal{S}(N)$ of constant energy density ρ and pressure P. N refers to the number of baryons enclosed by $\mathcal{S}$. We approximate the time derivative of the baryon density on a specific surface $\mathcal{S}(N)$ by the expression (Reisenegger & Goldreich 1992)

$$\frac{{\rm d}n}{{\rm d}t} \simeq \left.\frac{n}{n_{\rm c}}\right|_{\Omega=0}\frac{{\rm d}n_{\rm c}}{{\rm d}\Omega}\frac{{\rm d}\Omega}{{\rm d}t}, \tag{42}$$

where $n_{\rm c}$ is the central baryon density, and ${\rm d}n_{\rm c}/{\rm d}\Omega$ is obtained from calculations of rotating neutron star sequences (see Fig. 1).

The equilibrium value $x_{\rm eq}$ of the proton fraction is determined by the following condition on the energy per baryon E:

$$\begin{aligned}\delta\mu := \frac{\partial E}{\partial x} &= \frac{\partial E}{\partial n_{\rm p}}\frac{\partial n_{\rm p}}{\partial x} + \frac{\partial E}{\partial n_{\rm n}}\frac{\partial n_{\rm n}}{\partial x} + \frac{\partial E}{\partial n_{\rm e}}\frac{\partial n_{\rm e}}{\partial x} \\ &\quad + \frac{\partial E}{\partial n_{\mu}}\frac{\partial n_{\mu}}{\partial x} \qquad (43)\\ &= \mu_{\rm p} - \mu_{\rm n} + \mu_{\rm e} = 0, \qquad (44)\end{aligned}$$

where we used the charge neutrality of the system, $\partial n_{\rm p}/\partial x = \partial n_{\rm e}/\partial x + \partial n_{\mu}/\partial x$, the condition $\mu_{\rm e} = \mu_{\mu}$, and the equation $\partial n_{\rm p}/\partial x = -\partial n_{\rm n}/\partial x = n$. The time derivative of n is linked to the time derivative of $x^{\rm eq}$ by

$$\frac{{\rm d}x^{\rm eq}}{{\rm d}t} \simeq \frac{{\rm d}x^{\rm eq}}{{\rm d}n}\left.\frac{n}{n_{\rm c}}\right|_{\Omega=0}\frac{{\rm d}n}{{\rm d}\Omega}\frac{{\rm d}\Omega}{{\rm d}t}, \tag{45}$$

where Eq. (42) was used.

A deviation from chemical equilibrium corresponds to a non-vanishing value of $\delta\mu$. The non-vanishing gradient of the total chemical potential including both internal and external contributions causes a diffusion of particles. If the timescale for chemical relaxation is larger than the timescale for this diffusion, the chemical relaxation takes place in a larger regoin of the neutron star, and $\delta\mu$ has to be averaged over such regions.

It seems likely that this kind of relaxation occurs in the core of neutron stars (Reisenegger 1997).

The time derivative of

$$\delta\mu = \frac{\partial E}{\partial x} = \left.\frac{\partial^2 E}{\partial x^2}\right|_{x=x_{\rm eq}} (x - x_{\rm eq}) \tag{46}$$

yields the evolution equation for $\delta\mu$:

$$\frac{\partial \delta\mu}{\partial t} = \left.\frac{\partial^2 E}{\partial x^2}\right|_{x=x_{\rm eq}} \left(\frac{\Gamma}{n} - \frac{{\rm d}x^{\rm eq}}{{\rm d}n}\,\frac{n}{n_{\rm c}}\right|_{\Omega=0} \frac{{\rm d}n}{{\rm d}\Omega}\frac{{\rm d}\Omega}{{\rm d}t}\Bigg), \tag{47}$$

where $\Gamma(\delta\mu, n) = n\partial x/\partial t$ is the difference between the rates per unit volume of electron capture and beta decays. This difference gives a positive value for $\delta\mu > 0$, so that chemical equilibrium tends to be restored. The second derivative of the energy per baryon is equal to

$$\left.\frac{\partial^2 E}{\partial x^2}\right|_{x=x_{\rm eq}} = 8S(n) + \frac{1}{3}\hbar c(3\pi n)^{1/3} x^{-2/3}, \tag{48}$$

where $S(n)$ denotes the symmetry energy.

The average energy released by these reactions into kinetic and thus thermal energy is equal to the difference of the Fermi energies of protons and electrons on the one side and neutrons on the other side, i.e.:

$$h = \Gamma\delta\mu\,. \tag{49}$$

At the same time, thermal energy is lost by emission of thermal neutrinos, as it is the case for matter in chemical equilibrium. The emission rates are however modified by the deviation from chemical equilibrium (see Reisenegger & Goldreich 1992 for the values of Γ and ϵ_ν). Like the neutrino emissivity ϵ_ν, the reaction rate Γ is suppressed by superfluidity unless the deviation of chemical equilibrium $\delta\mu$ exceeds the sum of the gap energies of the participating baryons (Reisenegger 1997).

Until now we have considered only the restoration of chemical equilibrium in the core. The situation in the crust is similar, though more complex. Iida & Sato (1997) studied the Lagrangian changes in pressure associated with elements of matter due to the spin-down in the framework of the Hartle-approximation (Hartle 1967). By considering the nuclear processes induced above $\rho_{\rm l} = 3\times10^{13}\,{\rm g\,cm^{-3}}$ by compression or decompression of matter, they approximate the chemical energy per unit volume and time converted to thermal energy to

$$h \approx nqN\sin\theta|1 - 1.46\cos^2\theta|\frac{2\Omega|\dot\Omega|}{(6283\,{\rm s^{-1}})^2}\,, \tag{50}$$

where $nq \approx 4\,{\rm eV\,fm^{-3}}$ is the energy per unit volume released by one non-equilibrium process, $N \approx 15(\rho-\rho_{\rm l})/(\rho_{\rm tr}-\rho_{\rm l})$ is the number of processes in a unit cell, and $\rho_{\rm tr} = 1.7\times10^{14}\,{\rm g\,cm^{-3}}$ is the transition density between core and inner crust. By averaging over spherical shells we obtain

$$h \approx 3\times10^{21}\,\frac{\rho-\rho_{\rm l}}{\rho_{\rm tr}-\rho_{\rm l}}\,\frac{\Omega|\dot\Omega|}{1\,{\rm s^{-3}}}\,{\rm erg\,cm^{-3}\,s^{-1}}\,. \tag{51}$$

5. Additional ingredients and comparison of the efficiency of the heating mechanisms

Apart from the rates of the various heating processes discussed in the previous sections, some further ingredients are needed to solve the general relativistic equations of stellar structure and evolution (see Sect. 2.1). These additional ingredients are summarised in Table 1. Here we shall only discuss the equation of state of the dense interior of a neutron star, the neutrino emissivities, the superfluidity gaps and the photosphere, since these ingredients are the most important ones. Further, we will compare the efficiencies of the various heating mechanism.

5.1. Equation of state

For the outer and inner crust we adopt the equations of state of Haensel & Pichon (1994) and Negele & Vautherin (1973). The transition density between the ionic crust and the core of a neutron star is taken to be $\rho_{\rm tr} = 1.7\times10^{14}\,{\rm g\,cm^{-3}}$ (Pethick et al. 1995). For the present study, we choose two models of high density matter. The first, non-relativistic model (UV_{14}+UVII) is obtained by solving the Schrödinger equation by means of a variational approach (Wiringa et al. 1988). The other model (RHF8) uses relativistic Brückner-Hartree-Fock results up to 2–3 times normal nuclear density. Hyperons are included within the relativistic Hartree-Fock approach above this density (Huber et al. 1998). One important difference between these equations of state is that the non-relativistic model treat neutron star matter as being composed of neutrons and protons only (which are in β-equilibrium with leptons), whereas the relativistic model accounts for all hyperon states that become populated in the cores of neutron stars.

5.2. Neutrino emissivity

The neutrino emission processes can be divided into slow and enhanced processes depending on whether one or two baryons participate in the reaction. Due to the rather different phase spaces associated with both kind of processes the emission rates differ by several orders of magnitude.

If one neglects exotic states in neutron star matter (like quark-gluon plasma and meson condensates) the only enhanced neutrino emission processes are the direct nucleon and hyperon Urca processes

$$\mathrm{n} \;\rightarrow\; \mathrm{p} + \lambda^- + \bar\nu_\lambda \tag{52}$$

$$B_1 \;\rightarrow\; B_2 + \lambda^- + \bar\nu_\lambda, \tag{53}$$

respectively, where $B_{1,2} = $ n, p, $\Sigma^{\pm,0}$, Λ, $\Xi^{0,-}$ denotes the baryons and $\lambda_{1,2} = {\rm e}^-$, μ^- the leptons. Because of the β-equilibrium the inverse reaction (with $\bar\nu$ replaced by ν) occurs at the same rate as the direct one. The emissivities of these processes were computed by Prakash et al. (1992). Simultaneous conservation of energy and momentum requires that the triangle inequality $p^{\rm F}_{B_1} < p^{\rm F}_{B_2} + p^{\rm F}_{\rm e}$ and the two inequalities obtained by cyclic permutation are fulfilled for the Fermi momenta $p^{\rm F}_i$. If the inequalities are not fulfilled the process is ex-

Table 1. Input quantities used for the cooling simulations

Parameter	References
Equations of state:	
crust	Haensel & Pichon 1994, Negele & Vautherin 1973
core (alternatives)	
UV_{14}+UVII	Wiringa et al. 1988
RHF8	Huber et al. 1998
Superfluidity	see Table 2
Heat capacity	Shapiro & Teukolsky 1983, Van Riper 1991
Thermal conductivities:	
crust	Itoh et al. 1984, Itoh 1983, Mitake et al. 1984
core	Gnedin & Yakovlev 1995
Neutrino emissivities:	
pair-, photon-, plasma-processes	Itoh et al. 1989
bremsstrahlung in the crust	Yakovlev & Kaminker 1996, Haensel et al. 1996
bremsstrahlung in the core	Friman & Maxwell 1979, Kaminker et al. 1997
modified Urca	Friman & Maxwell 1979, Yakovlev & Levenfish 1995
direct nucleon Urca	Lattimer et al. 1991
direct hyperon Urca	Prakash et al. 1992
superfluid pair breaking	Voskresenskiĭ & Senatorov 1987, Schaab et al. 1997
Photosphere:	Potekhin et al. 1997

Table 2. Gap energies of superfluid states in neutron star matter. The density ranges are calculated for the RHF8 equation of state.

Pairing	$\Delta_{\max}$ [MeV]	Density range [fm^{-3}]	References
neutron $^1\mathrm{S}_0$	1.01	< 0.16	Schulze et al. 1996
proton $^1\mathrm{S}_0$	0.92	0.10–0.31	Elgarøy et al. 1996a
neutron $^3\mathrm{P}_2$	1.45	> 0.06	Baldo et al. 1998, CD-Bonn potential
lambda $^1\mathrm{S}_0$	0.24	0.44–0.63	Balberg & Barnea 1998

tremely unlikely to occur and the corresponding emissivity can be neglected. The availability of the various fast processes thus depends on the partial concentrations of each baryon species. The proton fraction, which determines the possibility of the direct nucleon Urca process, depends crucially on the symmetry energy, which is poorly known for high density matter. As an example of an equation of state which yields slow cooling we study the non-relativistic equation of state UV_{14}+UVII. Due to the non-monotonic behaviour of the symmetry energy at high densities, the triangle inequality is not fulfilled for this equation of state. The relativistic equation of state RHF8 allows for both the direct nucleon and the direct hyperon Urca processes for star masses $M > 1.09\,M_\odot$ and $M > 1.22\,M_\odot$, respectively.

During the transition to the superfluid state of neutrons and protons the superfluid pair breaking and formation processes become important (Flowers & Itoh 1976, Voskresenskiĭ & Senatorov 1987). We refer to Schaab et al. (1997) for a detailed description of these processes and their impact on the cooling of neutron stars.

5.3. Superfluidity

The pairing gaps are sensitive to the underlying microscopic model for the nucleon-nucleon interaction. Since these models are rather uncertain, especially at high densities, the value of the maximum gap and the density range where pairing can occur is model dependent. The disagreement arising from the different interaction models is enlarged by more subtle issues of the medium polarisation (Wambach et al. 1991, Schulze et al. 1996) or the inclusion of relativity (Elgarøy et al. 1996b).

At densities of the order $2 \times 10^{14}\,\mathrm{g\,cm^{-3}}$ the S state interaction becomes repulsive for neutrons, and the $^1S_0$ neutron gap closes. The attractive $^3P_2 - ^3F_2$ state interaction leads to the pairing in this channel at about the same densities. For the P state pairing we use the recent calculation of Baldo et al. (1998) which is based on the modern nucleon–nucleon CD-Bonn potential (Machleidt et al. 1996), which provides accurate fits to the actual nucleon-nucleon scattering data below 350 MeV.

Field theoretical descriptions of the heavy-baryon interaction based on the one-boson-exchange model indicate that the $\Lambda - \Lambda$ interaction has an attractive component. From the so-called doubly-strange hypernuclei, where two hyperons are bound in a single nucleus (Imai 1992), one can verify this field theoretical result, since, for instance, the separation energy of the two Λ hyperons, $B_{\Lambda\Lambda}$, exceeds the separation energy of a single Λ from the same nucleus, B_Λ, by more than a factor of two. As expected according to the quark model, the binding energy of hyperons, $\Delta B_{\Lambda\Lambda} \equiv B_{\Lambda\Lambda} - 2B_\Lambda \approx 4$–$5$ MeV, is somewhat less than the corresponding binding energy of nucleons, $\Delta B_{NN} \approx 6$–7 MeV. Due to these similarities, Λ hyperon pairing is expected in high density matter in analogy with the case of nucleons. Here, we use the Λ hyperon $^1\mathrm{S}_0$ gaps estimated by Balberg & Barnea (1998). The impact of Λ pairing on the thermal evolution of neutron stars has recently been investigated in Schaab et al. (1998a).

After the onset of the superfluid state of the respective constituents of stellar matter the neutrino emissivities, the thermal conductivity, and the heat capacity are suppressed by factors which behave like $\exp(-aT_\mathrm{c}/T)$ for $T \ll T_\mathrm{c}$, where T_c denotes the critical temperature and a is some constant of order unity (Maxwell 1979, Levenfish & Yakovlev 1994, Gnedin & Yakovlev 1995, Yakovlev & Levenfish 1995). We refer to Levenfish & Yakovlev (1994) for fitting formulas of $\mathcal{R}_\mathrm{sf}$, that are valid over the whole temperature range $T < T_\mathrm{c}$ for both types of pairing state. The suppression factor of the $^3\mathrm{P}_2$ pairing behaves exponentially only if the neutrons pair in the nodeless state with $m = 0$. In the case of $m = 2$ this factor behaves polynomially (Anderson & Morel 1961, Muzikar et al. 1980, Levenfish & Yakovlev 1994). The effects of $m = 2$ pairing on the cooling behaviour is discussed in Schaab et al. (1998b) where considerable modifications were found. Due to the uncertainty in of the ground state quantum numbers of the neutron condensate we shall adopt here the more conventional case of the $m = 0$ nodeless pairing.

5.4. Photosphere

While the heat conduction in the interior of the star is treated dynamically in our simulations the actual surface temperatures are obtained by attaching an outer envelope with $\rho \leq \rho_\mathrm{m}$ at the boundary to the 'core'. The validity of this approximation has been discussed in Gudmundsson et al. (1983). To obtain the surface temperatures we use the envelope calculations by Potekhin et al. (1997) whose non-magnetic photospheres provide a smaller gradient for low effective surface temperatures $T_\mathrm{eff} \lesssim 3 \times 10^5\,\mathrm{K}$ than the earlier calculations of Gudmundson et al. (1983) and Van Riper (1988), mainly due to a refined treatment of the electron conductivity in the non-degenerate region. This yields a slower cooling in the photon cooling era for stars older than $\gtrsim 10^6\,\mathrm{yr}$.

Even a rather small amount of accreted matter of say $\Delta M \sim 10^{-16} M_\odot$, substantially reduces the thermal insulation of the photosphere. The effect is highest for $\Delta M \sim 10^{-7} M_\odot$, where the accreted hydrogen is partly burned into helium and carbon. Additionally accreted matter will be converted into iron, leaving the thermal insulation of the star practically unchanged (Potekhin et al. 1997). The effect of accreted envelopes on cooling of neutron stars are discussed in Sect. 7.3.

5.5. Comparison of the efficiency of the heating mechanism

In Fig. 2 the heating rates

$$H = \int 4\pi r^2 \mathrm{e}^{\Lambda+2\phi} h \mathrm{d}r \tag{54}$$

discussed in Sect. 3 and 4 are compared with the total photon and neutrino luminosities L_γ and L_ν, respectively, where an isothermal configuration, i.e. $T\mathrm{e}^\phi = \mathrm{const.}$, is assumed. Since the heating rates depend not only on the temperature but also on the time, we use the standard thermal evolution scenario without heating to link the star's temperature to its age.

We use two values of the rotational parameter K (see Eq. (5)). About the first value, $K = 10^{-15}$ s (left panel in Fig. 2), the observed values of most of the pulsars scatter, particularly of the five pulsars in class A. However there are four pulsars (see Table 3) which are rather old, $\tau > 6 \times 10^7$ yr, and rotate very fast, $P < 6$ ms. These pulsars are supposed to be *recycled* by accretion of matter from a companion star (see, e.g., Lorimer 1996). Since their rotational parameter $K \sim 10^{-22}$ s is quite different from the one of all the other pulsars, we shall study them separately (see Sect. 7.4 and right panel of Fig. 2).

For the value $K = 10^{-15}$ s the rate of only three heating mechanism, EB- and PVB-pinning and corotating core, exceed both, the photon and the neutrino luminosities. We expect (and obtain) therefore only for these three heating mechanism a considerable effect (see Sect. 7). All these heating mechanism affect both the late and the early cooling. This is in contrast to the case, where $K = 10^{-22}$ s is employed. Since the time derivative of the angular velocity $\dot{\Omega}$ is small in the latter case, only the late cooling is affected. Besides the three heating mechanisms quoted above, the other heating mechanisms result in a heating rate which is larger than the photon luminosity, except the heating from a corotating crust. The rate of chemical heating of the core depends also on the deviation from chemical equilibrium and can be compared with the other processes only in detailed cooling simulations. As we will see in Sect. 7.4, it considerably affects the late cooling for $K = 10^{-22}$ s.

6. Observed data

Only a few of the known pulsars have been detected by the X-ray observatories Einstein, EXOSAT, ROSAT, and ASCA during the last two decades. We use a sample of 27 pulsars to compare the theoretical cooling curves with the observed data (see Table 3). Both the timing characteristics (i.e. Ω and $\dot{\Omega}$) and at least an upper limit on the effective surface temperature T_eff^∞ as measured at infinity are known for these pulsars. Table 3 summarises these data. The effective surface temperatures are specified together with their 2σ error range.

The ages of all pulsars except PSRs 0531+21 (Crab), 0833-45 (Vela) and 0002+62 are estimated via their spin-down age,

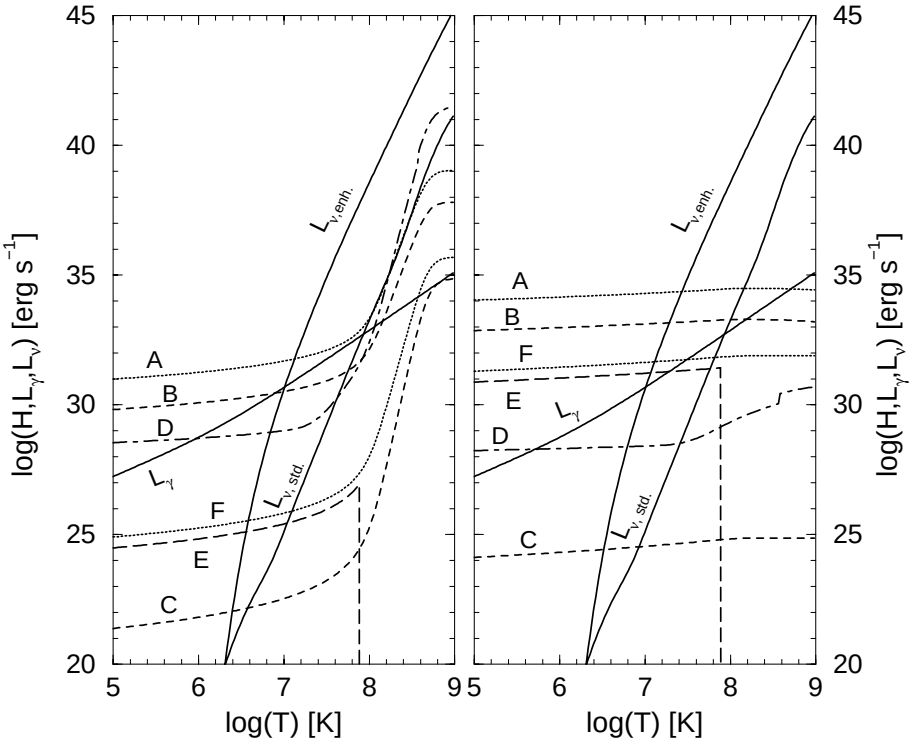

Fig. 2. Heating rate H as functions of internal temperature for A: EB-pinning, B: PVB-pinning, C: corotating crust, D: corotating core, E: crust cracking, F: chemical heating of the crust. The left panel corresponds to $K = 10^{-15}$ s, the right one to $K = 10^{-22}$ s. The photon luminosity, as well as the neutrino luminosity of a standard cooling and an enhanced cooling model are also shown.

$\tau = P/2\dot{P}$. This relation requires that both the moment of inertia and the magnetic surface field are constant, and that the braking index n is equal to its canonical value of 3, which corresponds to a spin-down by emission of pure magnetic dipole radiation (see Sect. 2.2). Of course, the spin-down age is a crude approximation to the true age of a neutron star, which can deviate from this value by a factor as large as ~ 3, as discussed before.

The situation is different for the three pulsars quoted above, where ages are known from different sources, that is: the age of the Crab pulsar is known from the chronicles, the age of Vela was recently determined via the proper motion of the pulsar with respect to the supernova remnant by Aschenbach et al. (1995), and the approximate age of PSR 0002+62 is given by an estimate of the age of the related supernova remnant G 117.7+06 (Hailey & Craig 1995).

The information obtained from the X-ray observations is not always sufficient to extract the effective surface temperature of the corresponding neutron star. The sample is therefore divided into four categories labelled A through D (Ögelman 1995, Schaab et al. 1996):

Category D: The four pulsars have not been detected in the soft X-ray range so far. By considering the instrumental sensitivity an upper limit for the surface temperature could be set. These pulsars are marked with white triangles in the figures below.

Category C: The detections of ten pulsars contain too few photons for spectral fits. The surface temperatures were obtained by using the totally detected photon flux. These pulsars are marked with black triangles.

Category B: The spectra of eight pulsars, including the Crab pulsar 0531+21, can only be fitted by a power–law–type spectrum or by a blackbody spectrum with very high effective temperatures and effective areas much smaller than a neutron star surface. Presumably, their X-ray emission is dominated by magnetospheric emission. Therefore, the temperatures, determined from the spectral fits, are probably higher than the actual surface temperatures. Pulsars of this type are marked with arrows.

Category A: Finally, there are five pulsars, 0833-45 (Vela), 0656+14, 0002+62, 0630+18 (Geminga), and 1055-52, which allow two–component spectral fits. The softer blackbody component is believed to correspond to the actual surface emission of the neutron star, while the harder blackbody (or power–law) component may be due to magnetospheric emission. These pulsars are marked with errorbars.

The obtained effective surface temperature of pulsars of category A depend crucially on whether or not a hydrogen atmosphere is assumed. PSR 0833-45 (Vela) is a specific example (cf. Table 3). Generally a spectral fit with a magnetic hydrogen atmosphere yields a substantially lower effective surface temperature than a blackbody fit. These models of hydrogen atmospheres however do not yet take into account the presence of neutral atoms (Potekhin et al. 1997). Their effect should yield a spectrum that is more similar to the blackbody spectrum, as indicated by the preliminary estimates by Shibanov et al. (1993). The atmospheric composition of a specific pulsar could be determined by considering multiwavelength observations in the near future (Pavlov et al. 1996). We shall use the effective surface temperatures obtained by fitting the spectra with both the blackbody and the magnetic hydrogen model atmosphere for

Table 3. Sample of observed data

Pulsar	P [ms]	$\dot{P}$ [$10^{-15}\,\mathrm{ss}^{-1}$]	$\log(\tau)$ [yr]	$\log(K)$ [s]	$\log(T_{\rm eff}^{\infty})$ [K]	Category	Reference
0531+21	33.40	420.96	2.97†	-13.9	$6.18^{+0.19}_{-0.06}$	B	1
(Crab)							
1509-58	150.23	1540.19	3.19	-12.6	6.11 ± 0.10	B	2
0540-69	50.37	479.06	3.22	-13.6	$6.77^{+0.03}_{-0.04}$	B	3,4
0002+62	241.81		~ 4†	~ -13	$6.20^{+0.07}_{-0.27}$	A,bb	5
0833-45	89.29	124.68	4.3 ± 0.3†	-14.0	6.24 ± 0.03	A,bb	6
(Vela)					5.88 ± 0.09	A,mH	7
1706-44	102.45	93.04	4.24	-14.0	$6.03^{+0.06}_{-0.08}$	B	8
1823-13	101.45	74.95	4.33	-14.1	6.01 ± 0.02	C	9
2334+61	495.24	191.91	4.61	-13.0	$5.92^{+0.15}_{-0.09}$	C	10
1916+14	1181	211.8	4.95	-12.6	5.93	D	11
1951+32	39.53	5.85	5.03	-15.7	$6.14^{+0.03}_{-0.05}$	B	12
0656+14	384.87	55.03	5.05	-13.7	5.98 ± 0.05	A,bb	13
					$5.72^{+0.06}_{-0.05}$	A,mH	14
0740-28	167	16.8	5.20	-14.6	5.93	D	11
1822-09	769	52.39	5.37	-13.4	5.78	D	11
0114+58	101	5.84	5.44	-15.2	5.98 ± 0.03	C	11
1259-63	47.76	2.27	5.52	-16.0	5.88	C	15
0630+18	237.09	10.97	5.53	-14.6	$5.76^{+0.04}_{-0.08}$	A,bb	16
(Geminga)					$5.42^{+0.12}_{-0.04}$	A,mH	17
1055-52	197.10	5.83	5.73	-14.9	$5.90^{+0.06}_{-0.12}$	A,bb	18
0355+54	156.38	4.39	5.75	-15.2	5.98 ± 0.04	C	19
0538+28	143.15	3.66	5.79	-15.3	5.83	C	20
1929+10	226.51	1.16	6.49	-15.6	5.52	B	21
1642-03	388	1.77	6.54	-15.2	6.01 ± 0.03	C	11
0950+08	253.06	0.23	7.24	-16.3	$4.93^{+0.07}_{-0.05}$	B	22
0031-07	943	0.40	7.56	-15.4	5.57	D	11
0751+18	3.47	7.9×10^{-4}	7.83	-20.6	5.66	C	23
0218+42	2.32	8.0×10^{-5}	8.66	-21.7	5.78	C	24
1957+20	1.60	1.7×10^{-5}	9.18	-22.6	5.53	C	25,26
0437-47	5.75	3.8×10^{-5}	9.20	-21.7	5.94 ± 0.03	B	27

The entries are: rotation period P, spin-down age $\tau = P/2\dot{P}$, $K = P\dot{P}$ (see Eq. (5)), effective surface temperature as measured at infinity $T_{\rm eff}^{\infty}$. The four categories A to D are explained in the text. bb and mH refer to blackbody and magnetic hydrogen atmosphere fits, respectively. †: estimated true age instead of spin-down age (see text). References: 1: Becker & Aschenbach 1995, 2: Seward et al. 1983k, 3: Finley et al. 1993, 4: Boyd et al. 1995, 5: Hailey & Craig 1995, Fig. 2 with lower limit on $N_{\rm H}$, 6: Ögelman 1995, Table III, 7: Page et al. 1996, Fig. 1, 8: Becker et al. 1995, 9: Finley & Ögelman 1993, 10: Becker et al. 1996a, 11: Slane & Lloyd 1995, 12: Safi-Harb & Ögelman 1995, 13: Possenti et al. 1996, 14: Anderson et al. 1993, 15: Becker et al. 1996b, 16: Halpern & Wang 1997, PSPC+SIS0, 17: Meyer et al. 1994, Fig. 2a with $B_{12} = 1.18$, 18: Greiveldinger et al. 1996, Table 2, 19: Slane 1994, 20: Sun et al. 1996, 21: Yancopoulos et al. 1994, 22: Manning & Willmore 1994, 23: Becker et al. 1996c, 24: Verbunt et al. 1996, 25: Kulkarni et al. 1992, 26: Fruchter et al. 1992, 27: Zavlin & Pavlov 1998.

the three pulsars of category A, for which both fits were accomplished.

7. Results and discussion

7.1. Standard cooling

Fig. 3 shows the surface temperature as measured by a distant observer as a function of the star's age for the slowly cooling neutron star models with and without internal heating. These models are based on the non-relativistic equation of state UV_{14}+UVII which account only for chemically equilibrated nucleons and leptons (cf. Sect. 5.1). We choose the canonical value $M = 1.4 M_{\odot}$ for the gravitational mass of a neutron star. Note that the relatively low surface temperature is caused by the inclusion of the superfluid pair breaking and formation process (Flowers et al. 1976, Voskresenskiĭ & Senatorov 1987, Schaab et al. 1997), which was not taken into account in the earlier investigations (e.g. Umeda et al. 1994; Page 1995a; Schaab et al. 1996). The standard cooling model without internal heating is consistent with most of the observations. A discrepancy occurs however for the effective surface temperature of the Vela pulsar 0833-45 derived for a blackbody fit, which tends to lie considerably above all cooling tracks. The effective radius obtained for the blackbody fit, i.e. $R_{\rm eff} \approx 6\,\mathrm{km}$, is considerably smaller than the canonical value of $\sim 10\mathrm{km}$, generally

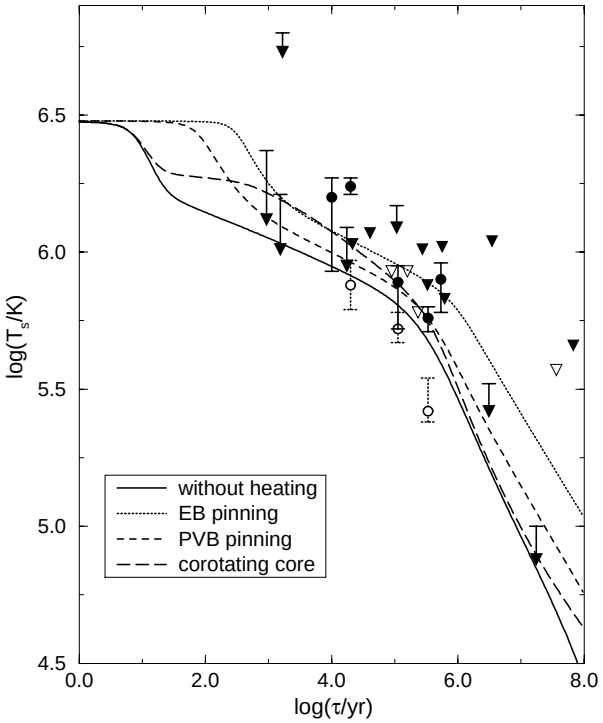

Fig. 3. Standard cooling with and without internal heating. Parameters are: UV_{14}+UVII equation of state, $M = 1.4 M_\odot$, and $K = 10^{-15}$ s. See Table 3 for the observed data.

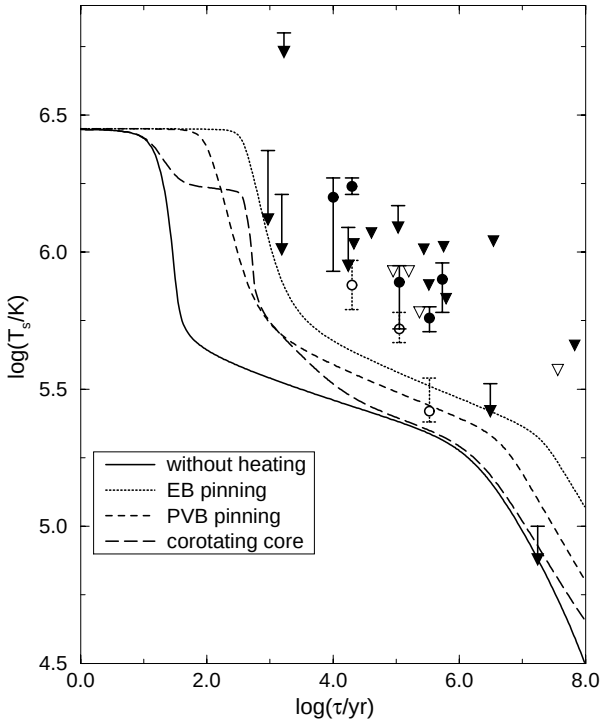

Fig. 4. Enhanced cooling of neutron star models constructed for the RHF8 equation of state. Other parameters are as in Fig. 3.

obtained for standard equations of state. Therefore, the existence of a magnetic hydrogen (or helium) atmosphere is more reliable and in agreement with the standard cooling scenario without internal heating.

The effect of heating of the crust due to thermal creep of pinned vortices is shown by the dotted and by the short dashed curves in Fig. 3 for the EB- and PVB-pinning model, respectively (see Sect. 3.1). The heating rate depends on $\dot{\Omega}$ (see Eq. [15]) and thus on the inverse of the magnetic dipole moment. The employed value $K = 10^{-15}$ s (see Eq. [5]) is in the range 10^{-16}–10^{-13} s about which the observed values tend to scatter, with the exception of the four millisecond pulsars which will be addressed in Sect. 7.4. The effective surface temperature is increased in both models in a similar way, though the effect of the EB-pinning model is larger because of the larger pinning energy in the inner crust. The heating of the crust can easily be recognised by the increase of the thermal diffusion time, i.e. by the amount of time needed for the cooling wave to reach the surface (Lattimer et al. 1994). After this time the surface temperature drops significantly. It is increased by a factor of ~ 50 (~ 10) in the case of EB- (PVB-)pinning. This characteristic feature will become very interesting if the thermal spectrum of a young pulsar $\tau \lesssim 100\,\mathrm{yr}$ should be detected.

For $\tau \gtrsim 10^6\,\mathrm{yr}$ the slope of the cooling track is increased by the heating of the crust. The observed upper limit of the effective surface temperature of PSR 0950+08 seems to rule out the EB-pinning model. Although consideration of a magnetic photosphere would decrease the slope again, compensation of the heating effect would require an unphysically strong magnetic field (Van Riper 1988). For middle aged pulsars, $10^3\,\mathrm{yr} < \tau < 10^6\,\mathrm{yr}$, heating due the PVB-pinning model has only a small effect compared to the other uncertainties of the input parameters.

The other three heating processes possible in the crust, driven by drag forces, crust cracking, and chemical heating have no visible effect on the cooling, since the heating rates are too small in comparison with the neutrino and photon emission rates (for the value of K used here). In the case of crust cracking our results are in contrast to the ones reported by Cheng et al. (1992), where a significant effect especially during the late cooling epoch has been obtained. This deviation can be traced back to different expressions used for the heating rates (see Sect. 4.1)

Electron-vortex scattering in the interior of the star affects the stellar cooling at times in the range $10^1 < \tau < 10^6\,\mathrm{yr}$ (see Fig. 3). During this period the effect is comparable to the effect of EB-pinning in the crust. Heating due to vortex decay at the crust-core boundary yields an increase of the surface temperature only for rather old pulsars ($\tau > 10^7\,\mathrm{yr}$). It can not be constrained by any present pulsar observation, however.

7.2. Enhanced cooling

Fig. 4 shows the cooling behaviour of enhanced cooling models which are based on the RHF8 equation of state. The surface temperature drops by a factor of ~ 6 when the cooling wave has reached the surface. The fast direct Urca processes are only suppressed below the critical temperature of neutron and lambda pairing, $T_\mathrm{c} \sim 2.0 \times 10^9$ K and $T_\mathrm{c} \sim 1.6 \times 10^9$ K, respectively.

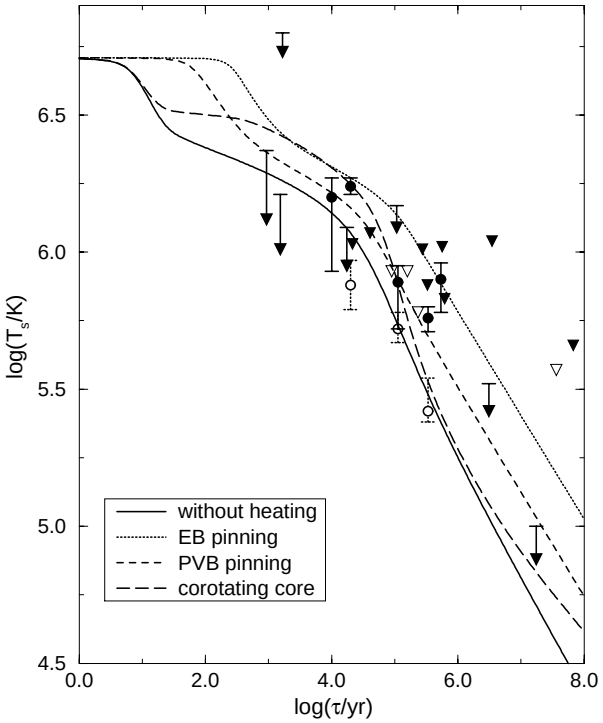

Fig. 5. Standard cooling with fully accreted envelope. Other parameters are as in Fig. 3.

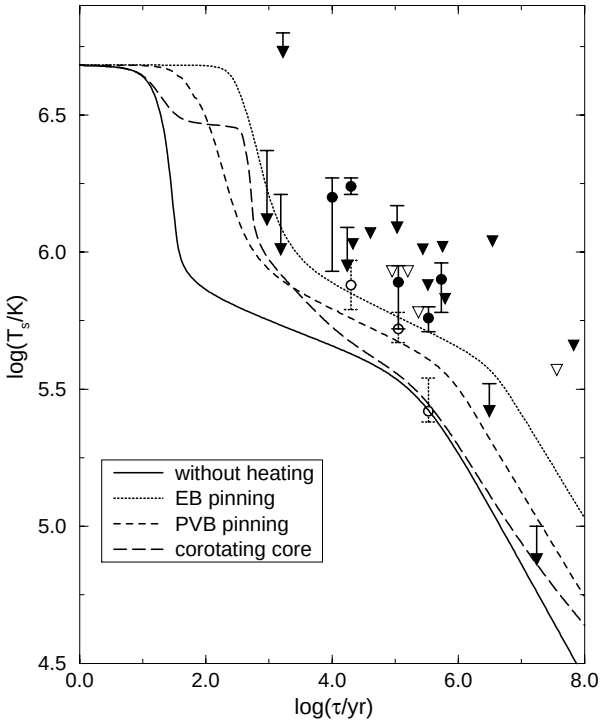

Fig. 6. Enhanced cooling with fully accreted envelope. Other parameters are as in Fig. 4.

The effect of heating on the cooling behaviour is similar as in the case of standard cooling. The EB-pinning model shows again the largest effect on the surface temperature.

With the only exception of PSR 0630+18 (Geminga), the effective surface temperatures of the pulsars of category A are clearly not consistent with the enhanced cooling models, no matter whether one includes heating processes or not. This discrepancy can be reduced either by enhancing the gap energies (Page 1995a, Schaab et al. 1996) or by assuming an accreted envelop.

7.3. Accretion

In Figs. 5 and 6, we study the effect of a fully accreted envelope, which means that the accreted mass exceeds $\sim 10^{-7} M_\odot$ (see Potekhin et al. 1997 and Sect. 5.4). Due to the envelope consisting of light atoms such as hydrogen, helium and carbon, the temperature gradient of the photosphere is substantially reduced. This yields a high effective surface temperature in the neutrino cooling era, during which the energy loss rate depends on the internal temperature; whereas it yields small surface temperatures in the photon cooling era where the loss rate depends on the surface temperature itself.

As it was already noted, the enhanced cooling models are now in better agreement with the data of observation class A (see Fig. 6). This is especially true for the surface temperatures obtained within the magnetic hydrogen atmosphere model. The enhanced cooling model with heating due PVB-pinning fits almost perfectly these surface temperatures.

7.4. Millisecond pulsars

So far we have investigated cooling scenarios associated with a large rotational parameter, i.e. $K = 10^{-15}$ s (see Eq. [5]). This value is consistent with the bulk fraction of observed pulsars (cf. Table 3). The four oldest pulsars, PSR 0751+18, 0218+42, 1957+20, and 0437-47, however have much smaller values around $K \sim 10^{-22}$ s. As it was shown in Sect. 5.5, this causes considerably different heating rates. In particular, the mechanism of chemical heating and crust cracking then becomes efficient enough to noticeably influence the thermal evolution. In Fig. 7 we show the results for the various heating mechanism in comparison with models without heating. Since the late cooling behaviour (for $\tau \gtrsim 10^7$ yr) does not depend on the cooling scenario, we consider here only the standard cooling scenario. The model with chemical heating of the core shows a sudden rise of the surface temperature at $\tau \sim 10^6$ yr. This is caused by the release of chemical energy through the β-decay of neutrons. This process is suppressed by superfluidity if the deviation from chemical equilibrium is smaller than the gap energy (s. Sect. 4.2 and Reisenegger 1997).

All cooling tracks in Fig. 7 are consistent with the upper temperature limits of the three oldest millisecond pulsars. Only the observation of PSR 0751+18 seems to exclude the EB-pinning model. The situation changes however if one assumes that the actual temperatures are not too far from the upper limits. Then only the PVB- and EB-pinning models, as well as the chemical heating of the superfluid core yield sufficiently high surface temperature. A future temperature determination, which will set a firm lower limit on the temperature for one of these pul-

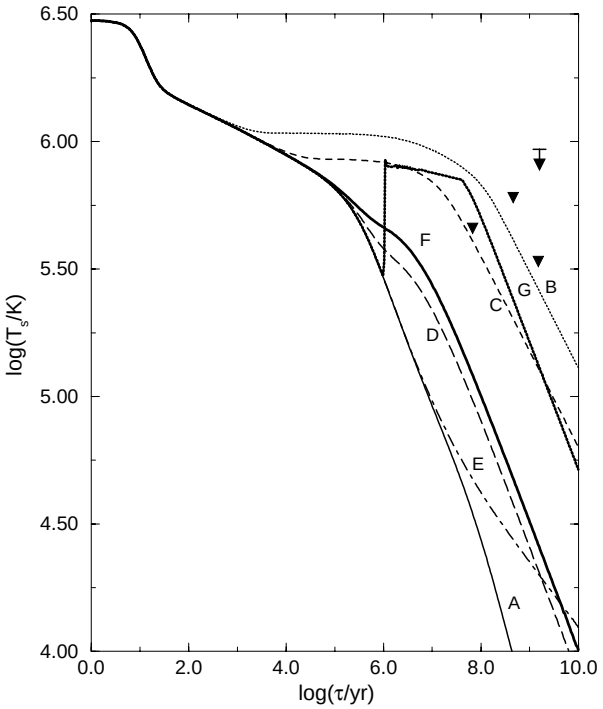

Fig. 7. Same as Fig. 3 but with various heating mechanism and $K = 10^{-22}$ s. The curves correspond to the models without internal heating (labeld with A), with EB-pinning (B), PVB-pinning (C), crust cracking (D), corotating core (E), chemical heating of the crust (F), and chemical heating of the core (G), respectively.

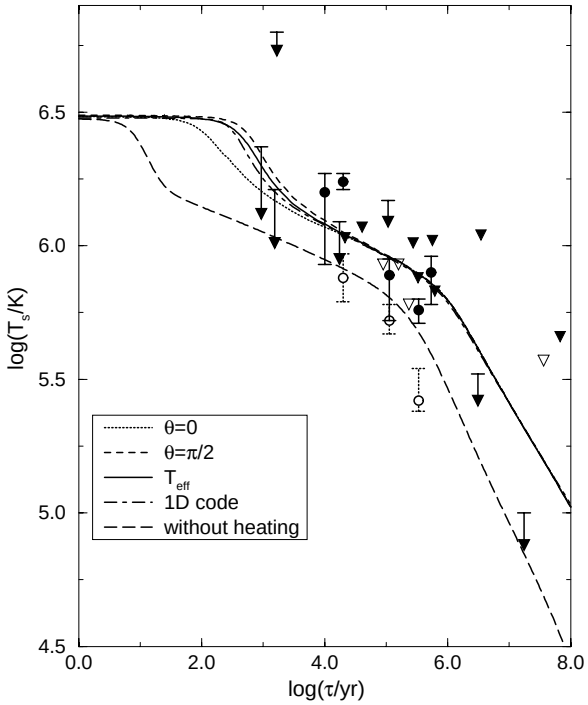

Fig. 8. Comparison of the one and two dimensional cooling simulations for the UV_{14}+UVII–model with inclusion of EB-pinning.

sars could therefore rule out at least the corotation and the crust cracking models as the only heat sources in millisecond pulsars.

7.5. Two dimensional simulations

In this section we relax the simplification that the heating rates are angle independent and extend our one-dimensional calculations of the previous sections to the two-dimensional case. The averaging of the local heating rates over spherical shells assumes that the heat conductivity is very high in transverse direction. This is indeed a fairly good approximation, as we shall see next by comparing the results of one dimensional calculation with those of fully two-dimensional ones. The two-dimensional code was developed recently by Schaab & Weigel (1998) (s.a. Schaab 1999).

Fig. 8 shows the obtained cooling tracks for standard cooling computed for the UV_{14}+UVII–model with inclusion of the EB-pinning model. Heating leads to a large temperature difference (up to 50 %) between the pole ($\theta = 0$) and the equator ($\theta = \pi/2$) for a pulsar whose age lies in the range $50 \lesssim \tau \lesssim 10^4$ yr. Moreover the temperature drop at the equator is delayed by the heating with respect to the model without heating and with respect to the drop of the polar temperature. This is the result of the $h \propto \sin\,\theta$ dependence for the vortex creep model.

The surface temperature obtained with the one dimensional code can be compared with the effective temperature which is defined by (Page 1995b)

$$T_{\rm eff} = \left(\int_0^1 {\rm d}s\; 2s\; \left({\rm e}^{\nu} T(\theta)\right)^4 \right)^{1/4}, \tag{55}$$

where $s = \sin\,\delta$. The emission angle δ is related to the colatitude θ by the equation

$$\theta(\delta) = \int_0^{M/R} {\rm d}u \frac{\sin\,\delta}{\left(\left(1 - \frac{2M}{R}\right) \left(\frac{M}{R}\right)^2 - (1-2u)u^2 \sin^2\,\delta \right)^{1/2}}, \tag{56}$$

where M and R are the neutron star's mass and radius, respectively. In flat spacetime, equation (56) simplifies to $\delta = \theta$.

The effective temperature $T_{\rm eff}$ and the surface temperature obtained with the one dimensional code are almost identical (see Fig. 8). This means that the luminosity obtained with both codes are also identical. The results of the one dimensional codes are thus acceptable for a comparison with the observed data of categories B–D, where the upper bounds on the surface temperature are derived from the respective luminosity. If one uses spectral information as for the pulsars in category A, the observations should be compared with the spectra derived from the surface temperature distribution $T_{\rm s}(\theta)$ in the framework of two dimensional simulations. Nevertheless, we expect that the conclusions remain unchanged if we use the effective temperature also for a comparison with the observed data of category A.

8. Conclusions

In this work, we have carried out a comparative analysis of the impact of different competing heating processes on the cooling

behaviour of neutron stars. In general we find that the internal heating yields significantly enhanced surface temperatures of middle aged and old pulsars, as one would expect. However, the effectiveness of these heating processes varies significantly from one process to another, and depends sensitively on the value of the rotational parameter K.

We studied models with two different rotational parameters. The first value was chosen to amount $K \sim 10^{-15}$ s, which is supported by pulsars observations. For this K value, the heating due to thermal creep of pinned vortices and motion of proton vortices in the interior of the star yield considerable enhancements of the surface temperatures of middle aged pulsars with respect to the models which ignore heating. This leads to closer agreement with the observed data in the case of enhanced cooling, which is even more improved for the case of the fully accreted envelopes (s.a. Page 1996).

The observed upper temperature limit for PSR 0950+08 seems to rule out the strong pinning models, whereas the weaker pinning models are consistent with the observations (the pinning models differ by the value of the pinning energy in the inner crust). The other heating processes – from chemical heating to dissipative motion of neutron vortices in the crust to crust cracking – have no observable effect on the cooling. Our result for heating due to crust cracking is in contrast to the one obtained by Cheng et al. (1992), who find a large effect especially on the late cooling stages. The difference arises from different expressions adopted for the heating rates.

The four oldest pulsars of our sample rotate very fast with periods of a few milliseconds. Hence the rotational parameter for millisecond pulsars is smaller than that for the bulk fraction of the population by 7 orders of magnitude ($K = 10^{-22}$ s). For this value only the late cooling stages are affected by heating. We find that the heating due to thermal creep of pinned vortices and chemical heating of the core has the largest impact on the surface temperatures of millisecond pulsars. Again, the strong pinning models leads to surface temperatures which are larger than one of the upper limits deduced for the millisecond pulsars.

As far as we know, the published cooling simulations of neutron stars which account for internal heating were performed in one spatial dimension. Such a treatment is only possible if the angle dependent heating rates are averaged over spherical shells. By comparing the outcome of one-dimensional simulations with fully two-dimensional simulations, based on a recently developed numerical code (Schaab & Weigel 1998), we could confirm the validity of this procedure.

The knowledge of the input parameters for cooling simulations such as the composition, the superfluid gap energies, and the possible existence of an accreted envelope, etc. is far form being complete. The number of parameters involved in the cooling simulations increases when the internal heating processes are taken into account. In principal, one could expect to derive some of the parameters associated with these phenomena by means of comparing the theoretical cooling models with the body of observed data. This attempt needs to be supplemented with the analysis of terrestical experiments, other astrophysical observations, as well as future theoretical studies. Nevertheless, the observed data already constrain the microphysical input, as, for instance, for the scenaria of heating via vortex creep.

Tables containing detailed references to the ingredients used in the simulations, the observational data, and the resulting cooling tracks can be found on the Web: http://www.physik.uni-muenchen.de/sektion/suessmann/astro/cool.

Acknowledgements. We would like to thank H.-T. Janka for helpful discussions and the anonymous referee for many valuable suggestions. Ch. S. gratefully acknowledges the Bavarian State for a fellowship. A. S. has been supported through a research grant from the Max Kade Foundation.

References

Alpar M.A., 1977, ApJ 213, 527
Alpar M.A., Anderson P.W., Pines D., Shaham J., 1984, ApJ 276, 325
Anderson P.W., Itoh N., 1975, Nat 256, 25
Anderson P.W., Morel P., 1961, Phys. Rev. 123, 1911
Anderson S.B., Cordova F.A., Pavlov G.G., Robinson C.R., Thompson, jr. R.J., 1993, ApJ 414, 867
Aschenbach B., Egger R., Trümper J., 1995, Nat 373, 587
Balberg S., Barnea N., 1998, Phys. Rev. C 57, 409
Baldo M., Elgarøy Ø., Engvik L., Hjorth-Jensen M., Schulze H.J., 1998, Phys. Rev. C 58, 1921
Baym G., Pines D., 1971, Ann. Phys. 66, 816
Becker W., Aschenbach B., 1995, In: Alpar M.A., Kiziloglu Ü., van Paradijs J. (eds.) The Lives of the Neutron Stars. Kluwer, Dordrecht, p. 47
Becker W., Brazier K.T.S., Trümper J., 1995, A&A 298, 528
Becker W., Brazier K.T.S., Trümper J., 1996a, A&A 306, 464
Becker W., Brazier K.T.S., Zavlin V.E., 1996b, Evidence for pulsed X-ray emission from the pulsar-Be star binary PSR 1259-63, submitted to MNRAS
Becker W., Trümper J., Lundgren S.C., Cordes J.M., Zepka A.F., 1996c, MNRAS 282, L33
Beskin V.S., Gurevich A.V., Istomin Y.N., 1984, Ap&SS 102, 301
Bildsten L., Epstein R.I., 1989, ApJ 342, 951
Blandford R.D., Applegate J.H., Hernquist L., 1983, MNRAS 204, 1025
Bonazzola S., Gourgoulhon E., Sagado M., Marck J., 1993, A&A 278, 421
Boyd P.T., Van Citters G.W., Dolan J.F., et al., 1995, ApJ 448, 365
Cheng K., Chau W., Zhang J., Chau H., 1992, ApJ 396, 235
Elgarøy Ø., Engvik L., Hjorth-Jensen M., Osnes E., 1996a, Nucl. Phys. A 604, 466
Elgarøy Ø., Engvik L., Hjorth-Jensen M., Osnes E., 1996b, Phys. Rev. Lett. 77, 1428
Epstein R.I., Baym G., 1988, ApJ 328, 680
Epstein R.I., Baym G., 1992, ApJ 387, 276
Finley J.P., Ögelman H., 1993, IAU Circ. No. 5787
Finley J.P., Ögelman H., Hasinger G., Trümper J., 1993, ApJ 410, 323
Flowers E., Itoh N., 1976, ApJ 206, 218
Flowers E., Ruderman M., Sutherland P., 1976, ApJ 205, 541
Friman B.L., Maxwell O.V., 1979, ApJ 232, 541
Fruchter A.S., Bookbinder J., Garcia M.R., Bailyn C.D., 1992, Nat 359, 303
Gnedin O.Y., Yakovlev D.., 1995, Nucl. Phys. A 582, 697
Goldreich P., Pacini A., Rees M.J., 1971, Ap&SS 3, 185
Greiveldinger C., Camerini U., Fry W., et al., 1996, ApJ 465, L35
Gudmundson E.H., Pethick C.J., Epstein R.I., 1983, ApJ 272, 286

Haensel P., 1992, A&A 262, 131
Haensel P., Pichon B., 1994, A&A 283, 313
Haensel P., Kaminker A.D., Yakovlev D.G., 1996, A&A 314, 328
Hailey C.J., Craig W.W., 1995, ApJ 455, L151
Halpern J.P., Wang F.Y.H., 1997, ApJ 477, 905
Hartle J.B., 1967, ApJ 150, 1005
Huber H., Weber F., Weigel M.K., Schaab C., 1998, Int. J. Mod. Phys. E 7, 301
Iida K., Sato K., 1997, ApJ 477, 294
Imai K., 1992, Nucl. Phys. A 547, 653
Itoh N., 1983, ApJ 273, 774
Itoh N., Kohyama Y., Matsumoto N., Seki M., 1984, ApJ 285, 758
Itoh N., Tomoo A., Nakagawa M., Kohyama Y., 1989, ApJ 339, 354
Jones P.B., 1990, MNRAS 246, 315
Jones P.B., 1992, MNRAS 257, 501
Kaminker A.D., Yakovlev D.G., Haensel P., 1997, A&A 325, 391
Kaspi V.M., Maschester R.N., Siegman B., Johnsten S., Lyne A.G., 1994, ApJ 422, L83
Komatsu H., Eriguchi Y., Hachisu I., 1989, MNRAS 237, 355
Kulkarni S.R., Phinny E.S., Evans C.R., Hasinger G., 1992, Nat 359, 300
Lattimer J.M., Pethick C., Prakash M., Haensel P., 1991, Phys. Rev. Lett. 66, 2701
Lattimer J.M., Van Riper K.A., Prakash M., Prakash M., 1994, ApJ 425, 802
Levenfish K.P., Yakovlev D.G., 1994, Pis'ma Astron. Zh. 20, 54
Link B., Epstein R.I., 1991, ApJ 373, 592
Link B., Epstein R.I., 1997, ApJ 478, L91
Link B., Epstein R.I., Baym G., 1993, ApJ 403, 285
Lorimer D., 1996, Physics World 9, 25
Lyne A.G., Pritchard R.S., Graham-Smith F., 1993, MNRAS 265, 1003
Machleidt R., Sammarruca F., Song Y., 1996, Phys. Rev. C 53, 1483
Manning R.A., Willmore A.P., 1994, MNRAS 266, 635
Maxwell O.V., 1979, ApJ 231, 201
Meyer R., Parlov G., Mészáros P., 1994, ApJ 433, 265
Mitake S., Ichimaru S., Itoh N., 1984, ApJ 277, 375
Mott N.F., Jones H., 1936, The Theory of the Properties of metals and Alloys. Oxford Univ. Press, Oxford
Muslimov A., Page D., 1996, ApJ 458, 347
Muzikar P., Sauls J., Serene J., 1980, Phys. Rev. D 21, 1494
Negele J., Vautherin D., 1973, Nucl. Phys. A 207, 298
Ögelman H., 1995, In: Alpar M., Kiziloglu Ü., van Paradijs J. (eds.) The Lives of the Neutron Stars. Kluwer, Dordrecht, p. 101
Page D., 1995a, Revi. Mex. Fís. 41, Supl. 1, 178
Page D., 1995b, Space Sci. Rev. 74, 437
Page D., 1996, ApJ 479, L43
Page D., 1998, In: Buccheri R., van Paradijs J., Alpar A. (eds.) The Many Faces of Neutron Stars. Kluwer, Dordrecht
Page D., Shibanov Y.A., Zavlin V.E., 1996, In: Röntgenstrahlung from the Universe: International Conference on X-Ray Astronomy and Astrophysics. MPE Report 263, 103, Max-Planck-Inst. Extraterr. Phys., Garching
Pavlov G., Zavlin V., Trümper J., Neuhäuser R., 1996, ApJ 472, L33
Pethick C., Ravenhall P., Lorenz C., 1995, Nucl. Phys. A 584, 675
Pizzochero P.M., Viverit L., Broglia R.A., 1997, Phys. Rev. Lett. 79, 3347
Possenti A., Mereghetti S., Colpi M., 1996, A&A 313, 565
Potekhin A.Y., Chabrier G., Yakovlev D.G., 1997, A&A 323, 413
Prakash M., Prakash M., Lattimer J., Pethick C., 1992, ApJ 390, L77
Reisenegger A., 1995, ApJ 442, 749
Reisenegger A., 1997, ApJ 485, 313
Reisenegger A., Goldreich P., 1992, ApJ 395, 240
Richardson M.B., Van Horn H.M., Ratcliff K.F., Malone R.C., 1982, ApJ 255, 624
Safi-Harb S., Ögelman H., 1995, ApJ 439, 722
Schaab C., 1999, Struktur und Thermische Entwicklung von Neutronensternen und Strange Sternen. GCA-Verlag, Herdecke, ISBN 3-928973-53-3, Ph.D. Thesis
Schaab C., Weigel M.K., 1998, A&A 336, L13
Schaab C., Weber F., Weigel M.K., Glendenning N.K., 1996, Nucl. Phys. A 605, 531
Schaab C., Voskresenskiĭ D., Sedrakian A.D., Weber F., Weigel M.K., 1997, A&A 321, 591
Schaab C., Balberg S., Schaffner-Bielich J., 1998a, ApJ 504, L99
Schaab C., Weber F., Weigel M.K., 1998b, A&A 335, 596
Schulze H.J., Cugnon J., Lejeune A., Baldo M., Lombardo U., 1996, Phys. Lett. B 375, 1
Sedrakian A., Cordes J.M., 1998a, ApJ 502, 378
Sedrakian A., Cordes J.M., 1998b, Vortex-Interface Interactions and Generation of Glitches in Pulsars, to be published in MNRAS, preprint astro-ph/9806042
Sedrakian A.D., Sedrakian D.M., 1993, ApJ 413, 658
Seward F.D., Harnden F.R., Murdin P., Clark D.H., 1983, ApJ 267, 698
Shapiro S.L., Teukolsky S.A., 1983, Black Holes, White Dwarfs and Neutron Stars. John Wiley & Sons
Shibanov Y.A., Zavlin V.E., Pavlov G.G., Ventura J., Potekhin A.Y., 1993, In: Van Riper K.A., Ho C., Epstein R. (eds.) Proc. Los Alamos Workshop, Isolated Pulsars. Cambridge Univ. Press, Cambridge, p. 174
Shibazaki N., Lamb F.K., 1989, ApJ 346, 808
Slane P., 1994, ApJ 437, 458
Slane P., Lloyd N., 1995, ApJ 452, L115
Smolukowski R., Welch D., 1970, Phys. Rev. Lett. 24, 1191
Sun X., Anderson S., Aschenbach B., et al., 1996, In: Zimmermann H.U., Trümper J.E., Yorke H. (eds.) Röntgenstrahlung from the Universe. International Conference on X-ray Astronomy and Astrophysics, Max-Planck-Inst. Extraterr. Phys., Garching, MPE Report 263, p. 195
Thorne K., 1977, ApJ 212, 825
Umeda H., Tsuruta S., Nomoto K., 1994, ApJ 433, 256
Van Riper K.A., 1988, ApJ 329, 339
Van Riper K.A., 1991, ApJS 75, 449
Van Riper K.A., Link B., Epstein R.I., 1995, ApJ 448, 294
Verbunt F., Johnston H.M., de Bryn G., van der Klis M., 1996, In: Bailes M., Johnston S., Walker M. (eds.) Proceedings of the IAU Colloqium 160
Voskresenskiĭ D.N., Senatorov A.V., 1987, Sov.J.Nucl.Phys. 45, 411
Wambach J., Ainsworth T.L., Pines D., 1991, In: Ventura J., Pines D. (eds.) Neutron Stars: Theory and Observation. Kluwer Academic Publishers, Dordrecht, Netherlands, pp. 37–48
Wiringa R., Fiks V., Fabrocini A., 1988, Phys. Rev. C 38, 1010
Yakovlev D.G., Kaminker A.D., 1996, Astron. Lett. 22, 491
Yakovlev D.G., Levenfish K.P., 1995, A&A 297, 717
Yancopoulos S., Hamilton T.T., Helfland D.J., 1994, ApJ 429, 832
Zavlin V.E., Pavlov G.G., 1998, A&A 329, 583